Supplementary Information

Operando-scanning electrochemical microscopic investigation and visualization

of NRR-HER competition in electrochemical NH₃ synthesis

Divyani Gupta,# Alankar Kafle,# Man Singh, Devyani Dahare and Tharamani C. Nagaiah *

Department of Chemistry, Indian Institute of Technology Ropar, Rupnagar, Punjab-140001, India

Email: tharamani@iitrpr.ac.in

Chemicals and reagents used

Analytical grade chemicals and reagents were used as such without further purification. Nickel nitrate ($Ni(NO_3).6H_2O$) and copper nitrate ($Cu(NO_3).6H_2O$) were purchased from Loba Chemie and sodium borohydride ($NaBH_4$, anhydrous) was purchased from Sigma-Aldrich. Hydrochloric acid (HCl, 37%) and sulfuric acid (H_2SO_4) were bought from Merck. Other chemicals viz. ammonium chloride (NH_4Cl, 99%), salicylic acid ($C_7H_6O_3$, 99.5%), sodium nitroprusside ($C_5FeN_6Na_2O$, 99%), para-dimethylaminobenzaldehyde ($p-C_9H_{11}NO$, 99%), sodium nitrate ($NaNO_3$, 99%), sodium nitrite ($NaNO_2$, 98%), sulphanilamide ($C_6H_8N_2O_2S$, 99%), N-(1-Napthyl) ethylenediamine dihydrocholoride ($C_{12}H_{14}N_2$, 99%), trisodium citrate ($Na_3C_6H_5O_7$) were bought from Loba Chemie. Reagents including sodium sulphate (Na_2SO_4, 99%) and potassium hydroxide (KOH, 85%), sodium hydroxide (NaOH, 98%), hydrazine monohydrate ($N_2H_4.H_2O$, 99%), sodium hypochlorite solution (NaClO, 4-6%) and hydrogen peroxide solution (H_2O_2, 5%) were also purchased from Loba Chemie. High purity $^{14}N_2$ (99.999%), $^{15}N_2$ (99%) and Ar gas (99.999%) cylinders were purchased from Sigma. All solutions were prepared using deionized water obtained from Millipore system (>15 MΩ).

Physical characterization

To examine the physicochemical properties of as-synthesized catalysts, a series of material characterizations were performed including P-XRD, SEM, FESEM, EDS, HR-TEM and XPS. PANalytical X'PERT pro diffractometer was used to perform P-XRD measurements in the 2θ range of 5-80° using Cu-Kα radiation (λ=0.1542 nm, 40kV, 40mA) at a low scan speed of 2° per minute. Scanning electron microscopy, field emission-scanning electron microscopy (Quanta 3D ESEM or

a JEOL (JEM-2800) microscope) and transmission electron microscopy (HR-TEM, JEOL, Jem 2100 plus) were utilized to analyse the morphology and topography of materials. The elemental composition was analysed using energy dispersive X-ray spectroscopic measurements (EDS, Oxford, INCAx-act, 51-ADD0013). The high resolution TEM (HR-TEM) images were recorded at 200 kV. XPS measurements were accomplished using Thermo scientific NEXSA surface analysis with a micro-focused (400 μm, 72 W, 12000 V) monochromatic Al Kα (1486.6 eV) hemispherical analyser and 128 channel plate detectors under ultrahigh vacuum (UHV 8-10 mbar). The obtained spectra were calibrated with C 1s spectra. Quantification of various impurities and products formed during NRR were tested using an (SEC2000-DH) UV-Vis Spectrometer. MP-AES analysis was carried out using Agilent 4200 Microwave Plasma Atomic Emission Spectrometer.

Electrochemical characterizations

The activity of catalysts towards NRR was analysed at room temperature in a home made two compartment H-cell, separated by a Nafion N117 membrane. Membrane was cleansed using the previously reported literature.[1] A three-electrode configuration was used to perform all the half-cell measurements equipped with glassy carbon (GCE Ø 2mm) as working electrode (WE), Ag/AgCl/3M KCl as reference electrode (RE) and graphite rod as counter electrode (CE) in 0.1 M H_2SO_4 electrolyte. Electrochemical characterizations such as CV, LSV, EIS and ECSA were performed using Biologic VSP 300 Potentiostat and Autolab 302N modular potentiostat/galvanostat and analysed by EC Lab and Nova 1.11 software respectively. The catalyst slurry in this study was prepared in 1:1 mixture of water: methanol (250 μL each) by taking 1.5 mg of catalyst powder (finely grinded in mortar pestle) under bath sonication for 15-

30 min. for homogeneous dispersion. Subsequently, the ink was drop-casted on GC electrode surface and dried under atmospheric conditions. Uncoated GCE was polished on a Nylon polishing cloth (SM 407052, AKPOLISH) prior drop-casting with alumina paste of different grades (0.5, 0.3, 0.05 μm; Pine instrument, USA) until mirror finishing is attained and then the electrode is washed and ultrasonicated in deionized water to remove any physiosorbed alumina particles. The charge transfer resistance was calculated using electrochemical impedance spectroscopy (EIS). A DC potential of -0.3 V vs. RHE was applied over an AC perturbation of 10 mV between a frequency range of 100 Hz to 40 KHz in a logarithmic frequency step over a single sine wave. The solution resistance (R_s) was obtained at high-frequency region, polarization resistance (R_p) was obtained at low-frequency region, wherein the difference between the two gave charge transfer resistance (R_{ct}) respectively. All these values were extracted from the semicircular behaviour of the Nyquist plot. The R_{ct} was uyilised thereafter to calculate the exchange current density. The double layer capacitance of electrocatalysts were evaluated by performing cyclic voltammetry at different scan rates (10 mV s^{-1} to 320 mV s^{-1}) under the non-faradaic region in 0.1 to 0.4 V *vs.* RHE in N_2-saturated 0.1 M H_2SO_4 solution. The average current density obtained from CVs were plotted against scan rate, wherein, the value of slope provided the double-layer pseudo-capacitance. ECSA was further calculated by dividing Cdl by specific capacitance of flat standard surface (40 μFcm^{-2}).[2]

SECM analysis

SECM measurements were executed using Sensolytics software and Autolab 204 N potentiostat (Metrohm) operated by Nova 1.11 software. A four-electrode system was used for the local

catalytic activity measurements, in which the tip used was a 10 μm diameter home-made gold ultramicroelectrode (Au-UME) with an RG value of around 5, which was determined using an optical microscope. The activity of Au-UME was tested in the redox solution containing 0.1 M KCl and 5mM of potassium hexacyanoferrate (II) trihydrate by means of cyclic voltammetry between -0.2 to 0.6 V *vs.* Ag/AgCl at 25 mV s^{-1}. Afterwards, the system was prepared for analysis where the GC plate was used as a substrate and WE2, Au-UME was used as WE1, Ag/AgCl/3M KCl was used as RE and coiled Pt was the CE respectively. The SECM cell was assembled and then connected to a bipotentiostat and then the approach curves were taken at three different positions surrounding the catalyst spot on GC plate (scan area equal to 1200 x 1200 μm). The Au-UME tip was kept at a constant XY position and the Z position was brought closer to catalyst spot using piezo motors and then the tilt correction was performed. In order to study the ability of catalyst towards NRR and its competition with HER a series of experiments including CV and CA were performed. The electrolyte solution i.e. Ar- and N_2-saturated 0.1 M H_2SO_4 was poured in the empty cell to carry out HER and NRR respectively. The CVs were acquired for known concentration of ammonia to choose the potential for its oxidation. Sample generation-tip collection mode (SG-TC) mode of SECM was employed to visualize the local catalytic activity of catalyst towards NRR and HER. The substrate was polarized with the potential at which NRR can take place (-0.3 V) while the tip was oxidised at ammonia oxidation potential (1.1 V *vs.* RHE). The SECM scans were carried out over catalyst spot in a fixed are of 1200 x 1200 μm at tip offset of 10 μm which yielded 36 acquisition points per line and the scan lasted for about 2 h. The obtained CA graphs were plotted using Origin 9.0 software while the SECM scans were extracted using Gwyddion 2.60 software.
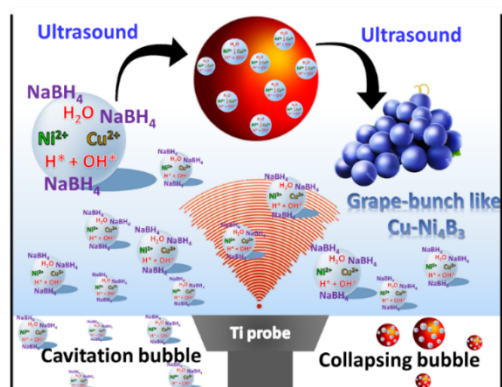
Fig. S1A Schematic representation of synthesis of catalyst via one step sonochemical reduction method.
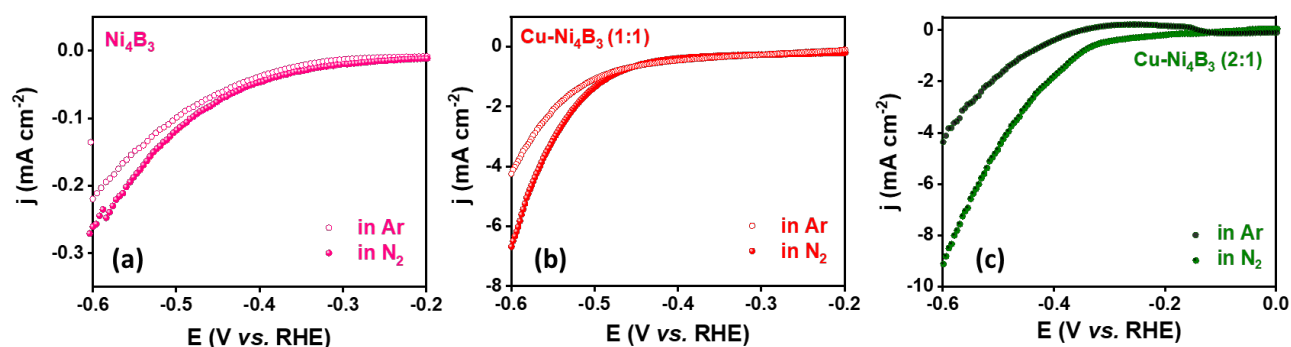

Fig. S1B LSV curves recorded for (a) Ni_4B_3, (b) $Cu-Ni_4B_3$ (1:1) and (c) $Cu-Ni_4B_3$ (2:1) catalysts respectively under Ar- and N_2-saturated 0.1 M H_2SO_4 electrolyte.

Table S1. NRR activity comparison of Ni_4B_3 and $Cu-Ni_4B_3$ catalysts extracted from respective LSV curves.

S. No.	Electrocatalyst	Onset potential (V *vs.* RHE) @ -0.5 mA cm^{-2}	Current density (mA cm^{-2}) @ -0.6 V
1.	Ni_4B_3	-	-0.28
2.	$Cu-Ni_4B_3$ (1:1)	-0.43	-6.8
3.	$Cu-Ni_4B_3$ (1:2)	-0.30	-17.2
4.	$Cu-Ni_4B_3$ (2:1)	-0.32	-9.1

S. No.	Electrocatalyst	Onset potential (V *vs.* RHE) @ -1.0 mA cm^{-2}	Current density (mA cm^{-2}) @ -0.6 V
1.	Ni$_4$B$_3$	-	-0.28
2.	Cu-Ni$_4$B$_3$ (1:1)	-0.48	-6.8
3.	Cu-Ni$_4$B$_3$ (1:2)	-0.34	-17.2
4.	Cu-Ni$_4$B$_3$ (2:1)	-0.36	-9.1

S. No.	Electrocatalyst	Onset potential (V *vs.* RHE) @ -0.5 mA cm^{-2}	Current density (mA cm^{-2}) @ -0.6 V
1.	Ni$_4$B$_3$	-0.59 @-0.25 mA cm^{-2}	-0.28
2.	Cu-Ni$_4$B$_3$ (1:1)	-0.43	-6.8
3.	Cu-Ni$_4$B$_3$ (1:2)	-0.30	-17.2
4.	Cu-Ni$_4$B$_3$ (2:1)	-0.32	-9.1
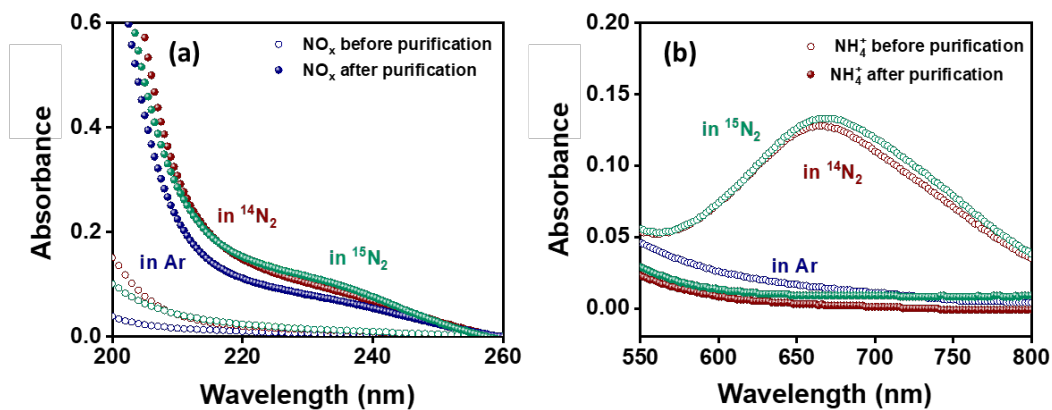
Fig. S2 UV-Vis. absorbance curves for (a) NO$_x$ and (b) NH$_4^+$ impurities in commercial gas-supplies viz. Ar, ^{14}N$_2$ and ^{15}N$_2$ before and after purification.

Table S2. Quantification of NO_x/NH_4^+ impurities in commercial gas-supplies by colorimetric and GC-MS techniques.

S. No.	Commercial gas feed	Before purification			After purification		
		NO/NO$_2$	N$_2$O	NH$_4^+$	NO/NO$_2$	N$_2$O	NH$_4^+$
1.	Ar	0.6 ppm	<0.01 ppm	NA	NA	NA	NA
2.	$^{14}N_2$	1.1 ppm	0.06 ppm	0.09 ppm	<0.01 ppm	<0.01 ppm	NA
3.	$^{15}N_2$	1.2 ppm	0.07 ppm	0.08 ppm	<0.01 ppm	<0.01 ppm	NA
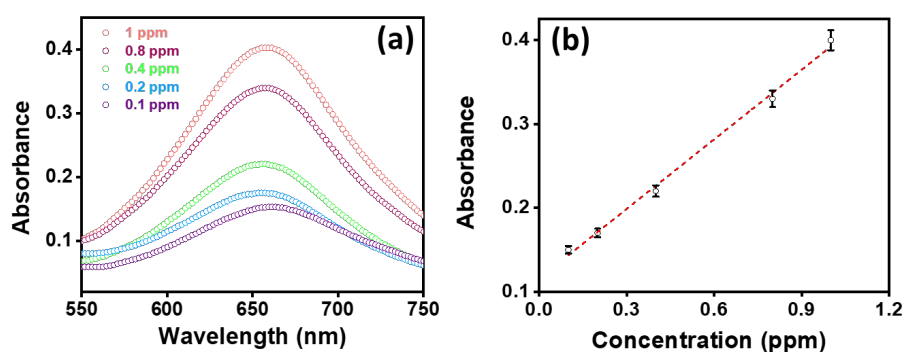
Fig. S3 UV-Vis absorbance curves for (a) standard NH_4^+ samples with varying concentrations and (b) corresponding standard calibration curve extracted from the same.
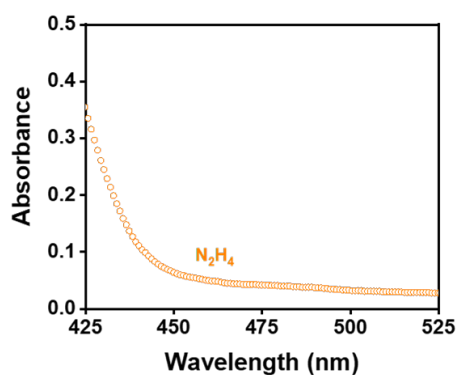
Fig. S4 UV-Vis curves obtained after NRR by Cu-Ni$_4$B$_3$ (1:2) shows the absence of hydrazine by-product.

**Table S3.** Comparison with recent literature on NRR by non-noble TM based catalysts

Catalyst	Electrolyte	NH$_3$ yield rate	FE (%)	Potential (V vs. RHE)	Ref.
MoO$_3$ nanosheets	0.1 M HCl	29.43 µg h^{-1} mg$_{cat.}^{-1}$ (-0.5 V)	1.9 (-0.3 V)	-	[3]
Cu dendritic	0.1 M HCl	25.63 µg h^{-1} mg$_{cat}^{-1}$	15.12	-0.40	[4]
NC-Cu SA	0.1 M HCl	49.3 µg h^{-1} mg$_{cat.}^{-1}$	11.7	-0.3	[5]
d-TiO$_2$ nanobelts	0.1 M HCl	1.2×10^{-10} mol s^{-1} cm^{-2}	9.2	-0.5	[6]
α-Mo$_2$C	0.5 M H$_2$SO$_4$	3.36 µg h^{-1} cm^{-2}	40.2	-0.55	[7]
Fe$_{0.4}$Ni$_{1.6}$P	0.1 M HCl	88.51 µg h^{-1} mg$_{cat}^{-1}$	7.92	-0.3	[8]
Cu	0.1 M HCl	24.5 nmol s^{-1} cm^{-2} (-0.4 V)	18 (-0.35 V)	-	[9]
Fe-SnO$_2$	0.1 M HCl	82.7 µg h^{-1} mg$_{cat.}^{-1}$	20.4	-0.3	[10]
CuS	0.1 M HCl	18.18 µg h^{-1} mg$_{cat}^{-1}$	5.63	−0.15	[11]
10%Ce-Bi$_2$WO$_6$	0.1 M HCl	22.5 µg h^{-1} mg$_{cat}^{-1}$	15.9 %	-0.2	[12]
Mn-O$_3$N$_1$/PC	0.1 M HCl	66.41 ± 4.05 µg h^{-1} mg$_{cat.}^{-1}$	8.91 ± 0.82	-0.35	[13]
MoO$_{3-x}$/MXene	0.1 M HCl	95.8 µg h^{-1} mg$_{cat}^{-1}$	22.3	−0.4/−0.3	[14]
Ti$_2$N nitride MXene	0.1 M HCl	11.33 µg h^{-1} mg$_{cat}^{-1}$	19.85	−0.25	[15]
Zn^{1}N–C	0.1 M HCl	16.1 µg h^{-1} mg$_{cat}^{-1}$	11.8	−0.3	[16]
OV-Ti$_2$O$_3$	0.1 M HCl	37.24 µg h^{-1} mg$_{cat}^{-1}$	19.29	−0.25	[17]
Cu$_3$P	0.1 M HCl	18.9 µg h^{-1} mg$_{cat}^{-1}$	37.8	−0.2	[18]
Fe$_1$S$_x$@TiO$_2$	0.1 M HCl	18.3µg h^{-1} mg$_{cat.}^{-1}$	17.3	-0.2	[19]
d-AuNCs/ Ti$_3$C$_2$T$_x$	0.1 M HCl	88.3±1.7 µg h^{-1} mg$_{cat.}^{-1}$	9.3±0.4 %	-0.35	[20]
1T/2H MoSSe	0.1 M HCl	32.32 µg h^{-1} mg$_{cat.}^{-1}$ (-0.45 V)	12.66% (-0.40 V)	-	[21]
Cu-Ni$_4$B$_3$ (1:2)	**0.1 M H$_2$SO$_4$**	**684 µg$_{NH3}$ h^{-1} mg$_{cat.}^{-1}$**	**43.42%**	**-0.3**	**This work**
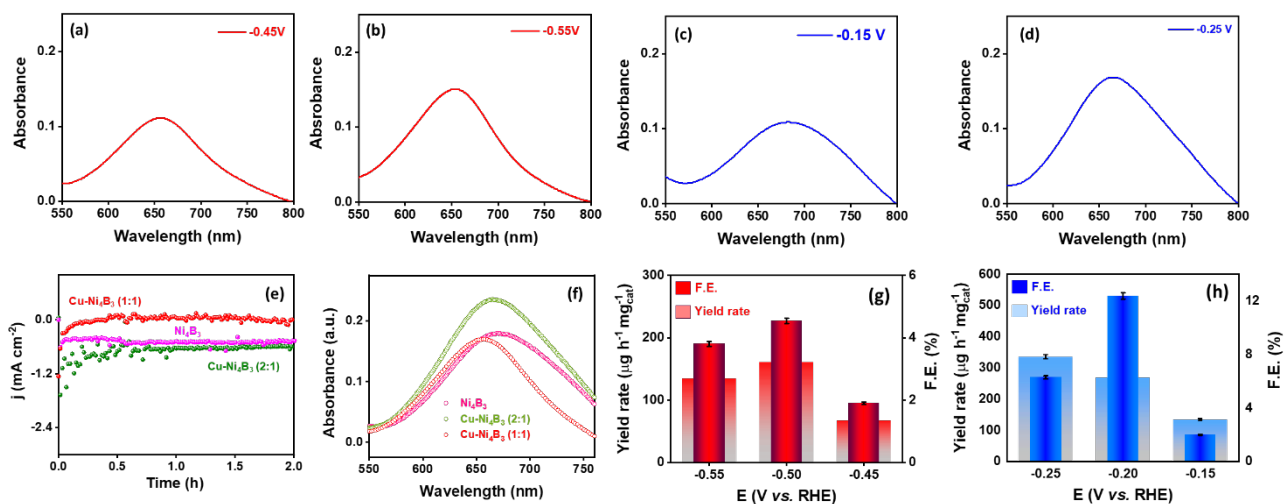
Fig. S5A (a) UV-Vis absorbance curves after NRR at different potentials by (a-b) Cu-Ni$_4$B$_3$ (1:1), (c-d) Cu-Ni$_4$B$_3$ (2:1) catalyst, (e) chronoamperometric measurements carried out at -0.45, -0.5 and -0.2 V (*vs.* RHE) for Ni$_4$B$_3$, Cu-Ni$_4$B$_3$ (1:1) and Cu-Ni$_4$B$_3$ (2:1) for 2 h under N$_2$-saturated 0.1 M H$_2$SO$_4$, (f) UV-Vis absorbance curves after NRR by different catalysts showing the production of ammonia. Bar graph comparison of F.E. and NH$_3$ yield rate of (g) Cu-Ni$_4$B$_3$ (1:1) and (h) Cu-Ni$_4$B$_3$ (2:1) catalyst at different applied potentials in N$_2$-saturated 0.1 M H$_2$SO$_4$.
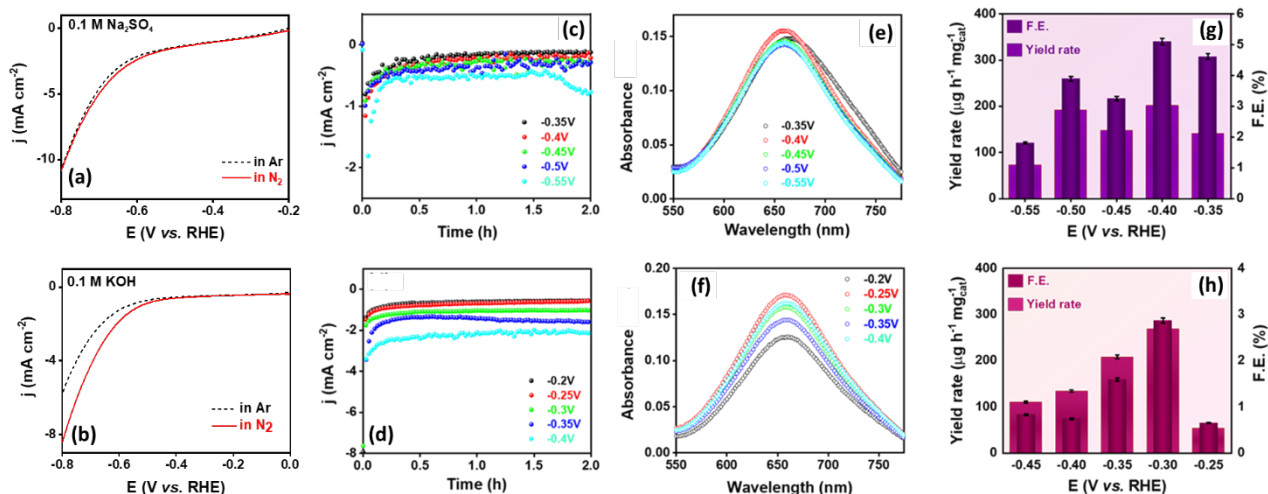
Fig. S5B (a-b) LSV curves, (c-d) chronoamperometric curves recorded for Cu-Ni$_4$B$_3$ (1:2) catalyst at different potentials in 0.1 M Na$_2$SO$_4$ and 0.1 M KOH respectively. (e-f) UV-Vis absorbance curves obtained for samples collected after NRR by optimized catalyst in neutral and alkaline conditions and (g-h) bar graph representing the subsequent ammonia production yield rate and F.E. towards NRR by Cu-Ni$_4$B$_3$ (1:2) in 0.1 M Na$_2$SO$_4$ and 0.1 M KOH consequently.
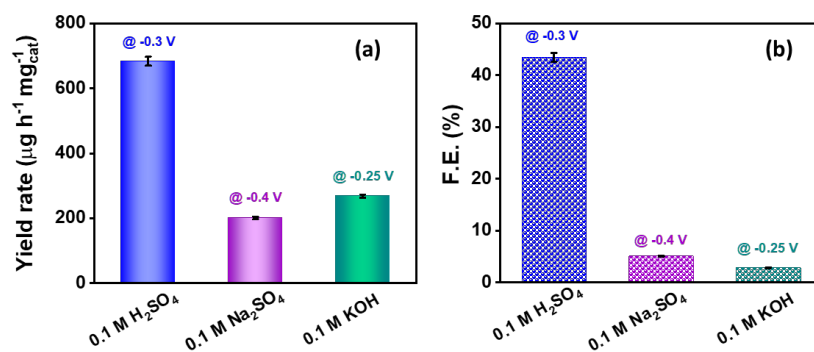

**Fig. S5C** (a) NH$_3$ yield rate and (b) F.E. after NRR by Cu-Ni$_4$B$_3$ (1:2) in different electrolytes.

Collection efficiency of Au-UME:

The determination of the maximum collection efficiency was executed using a redox mediator *i.e.* potassium hexacyanoferrate (Fe^{2+} → Fe^{3+}). It should be noted here that the Au-UME tip was

mechanically polished prior the collection efficiency determination to avoid any possible effects from the gold corrosion induced by hexacyanoferrates.[22] Initially, the Au-UME was positioned above the catalyst coated substrate (centre of the spot under the condition d/a= 1) and LSV of the substrate was recorded while the tip potential was held at a constant value where the substrate generated species reacts under diffusion controlled conditions at a low scan rate to allow steady-state concentrations to be achieved. In presence of redox mediator (5 mM $K_4[Fe(CN)_6]$) in 0.1 M H_2SO_4, the experimental conditions for SG-TC mode were E_{tip}= 0.4 V and $E_{substrate}$ = -0.2 to 0.5 V respectively. The LSV curves shown in Fig. S6A depict the experimental results of SG-TC SECM using redox mediator with oxidation at substrate and reduction at tip for the calculation on CE as a function of d/a. From the as-obtained steady-state tip and substrate currents, the CE is calculated at *d/a*= 1 by the ratio between the tip and the substrate current. The CE value has come out to be 58.6% for the Au-UME under the applied conditions.
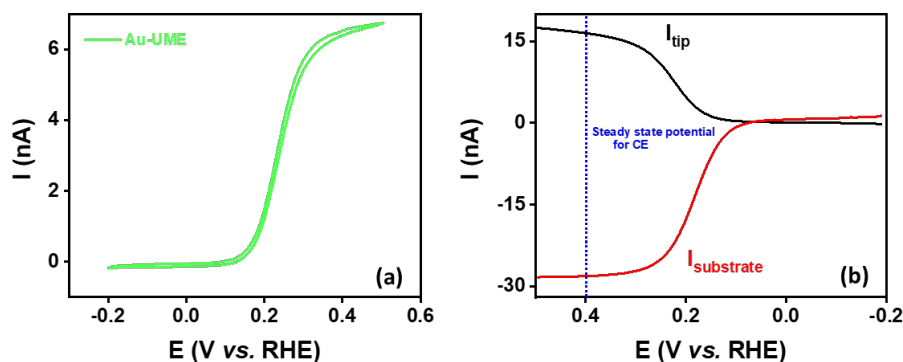

Fig. S6A (a) CV recorded at Au-UME tip in redox mediator 5 mM $K_4[Fe(CN)_6]$ to see the activity of electrode before measurements and (b) experimental results of the SG-TC SECM using 5 mM $K_4[Fe(CN)_6]$ oxidation at tip and reduction at substrate (after subtracting the background currents) for calculation of CE as a function of *d/a*=1.
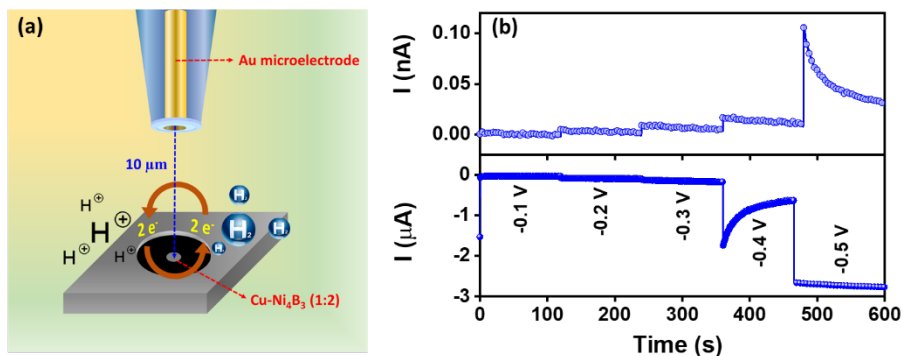
Fig. S6B (a) Schematic representation of SG-TC mode in SECM employed for qualitative H_2 estimation. (b) Sequential chronoamperometry curves recorded by polarizing the WE1 Au-tip at 1.1 V while scanning WE2 from -0.1 to -0.5 V (*vs*. RHE) for 120 s in Ar-saturated 0.1 M H_2SO_4.
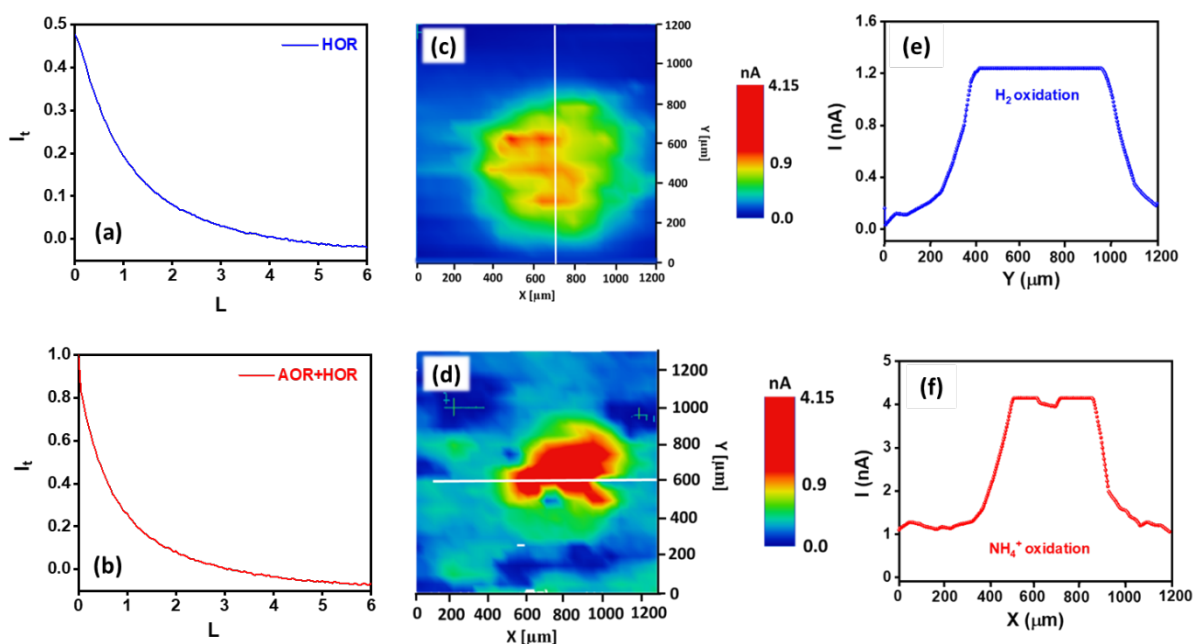

Fig. S7A (a-b) Approach curves, (c-d) 2D SG-TC SECM images and (e-f) corresponding line scan extracted from array scan for HOR and AOR+HOR at Au-UME by HER and NRR+HER over Cu-Ni$_4$B$_3$ (1:2) catalyst at a WE2 potential of -0.3 V *vs.* RHE where WE1 was fixed at 1.1 V (*vs.* RHE) to collect and oxidise the produced H_2 and NH_4^+ in the 10 μm gap between sample-to-tip in Ar- and N_2-saturated 0.1 M H_2SO_4 electrolyte employing SG-TC mode of SECM.
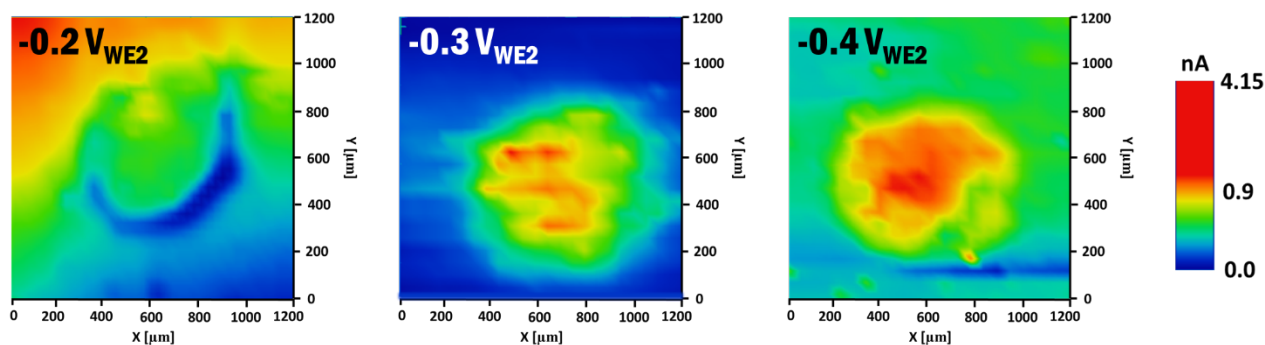
Fig. S7B 2D SG-TC SECM images for the HER over the Cu-Ni$_4$B$_3$ (1:2) catalyst at different WE2 potentials ranging between -0.2 to -0.4 V *vs.* RHE where WE1 was fixed at 1.1 V (*vs.* RHE) to collect and oxidise the produced H$_2$ in the 10 μm gap between sample-to-tip in Ar-saturated 0.1 M H$_2$SO$_4$ electrolyte.
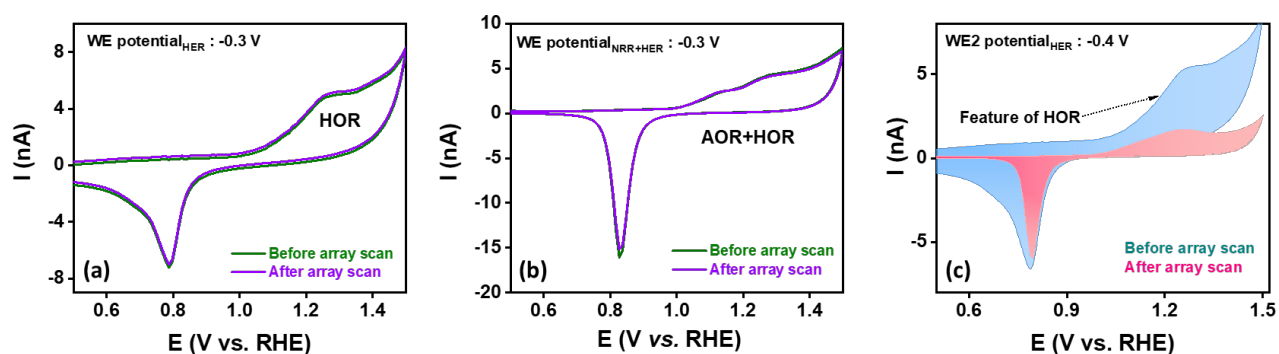

Fig. S7C Cyclic voltammograms recorded on Au-tip electrode before and after SG-TC SECM array scans when the substrate was polarized with a constant potential of -0.3 V (*vs.* RHE) in 0.1 M H$_2$SO$_4$ electrolyte showing the (a) HOR and (b) AOR+HOR. CV curves showing behaviour of Au-UME before and after SG-TC SECM array scans towards HOR when substrate was biased with -0.4 V of potential to produce H$_2$ at catalyst in Ar-saturated 0.1 M H$_2$SO$_4$ electrolyte.
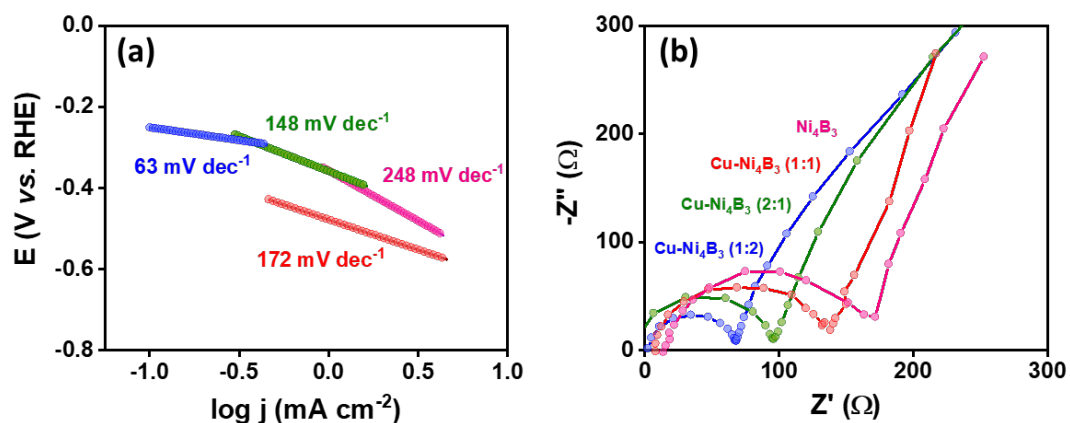
Fig. S8 (a) Tafel plots acquired for catalysts extracted from their respective LSV curves in N₂-saturated 0.1 M H_2SO_4 electrolyte and (b) Nyquist plots for $Cu-Ni_4B_3$ catalysts and Ni_4B_3 obtained after EIS measurements at a formal redox potential of 0.3 V (*vs.* RHE) for 5 mM potassium ferrocyanide in 0.1 M H_2SO_4 electrolyte.

Table S4A. EIS analysis of Ni_4B_3 and $Cu-Ni_4B_3$ catalysts.

| S. No.	Electrocatalyst	R_s (Ω)	R_p (Ω)	R_{ct} (Ω)	Exchange current density (j_o)
1.	Ni_4B_3	14	169.71	155.71	0.87 mA cm^{-2}
2.	$Cu-Ni_4B_3$ (1:1)	7.38	137.93	130.55	1.04 mA cm^{-2}
3.	$Cu-Ni_4B_3$ (1:2)	1.84	68.7	66.86	2.03 mA cm^{-2}
4.	$Cu-Ni_4B_3$ (2:1)	6.22	97.93	91.71	1.49 mA cm^{-2}
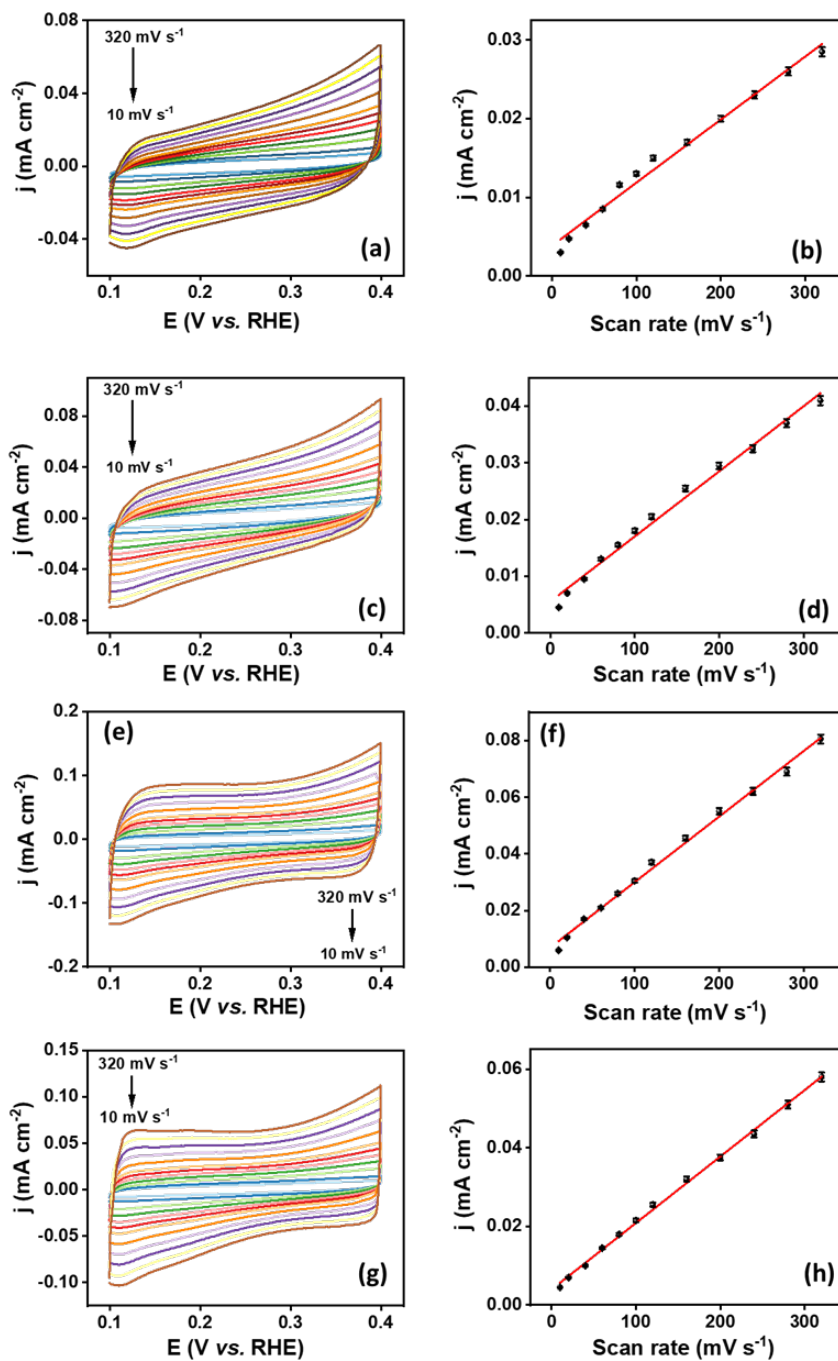
Fig. S9 (a), (c), (e), (g) Cyclic voltammograms acquired in non-faradaic region and (b), (d), (f), (h) corresponding linear plots of scan rate *vs.* current density for Ni_4B_3, $Cu-Ni_4B_3$ (1:1), $Cu-Ni_4B_3$ (1:2) and $Cu-Ni_4B_3$ (2:1) respectively.
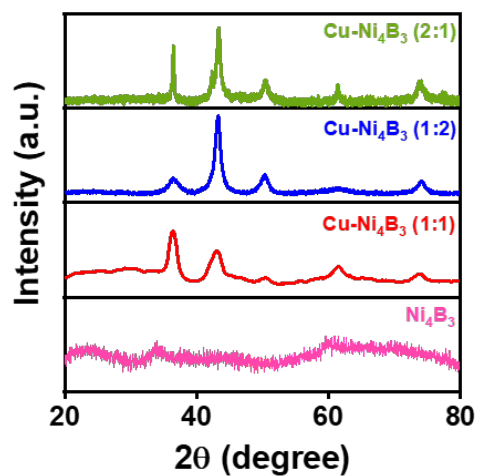
**Table S4B.** ECSA determination for Cu-Ni$_4$B$_3$ catalysts.

| S.No.	Electrocatalyst	C_{dl}* (mF)	ECSA (cm^2)
1.	Ni$_4$B$_3$	0.8	2
2.	Cu-Ni$_4$B$_3$ (1:1)	1.14	2.85
3.	Cu-Ni$_4$B$_3$ (1:2)	2.31	5.775
4.	Cu-Ni$_4$B$_3$ (2:1)	1.89	4.725
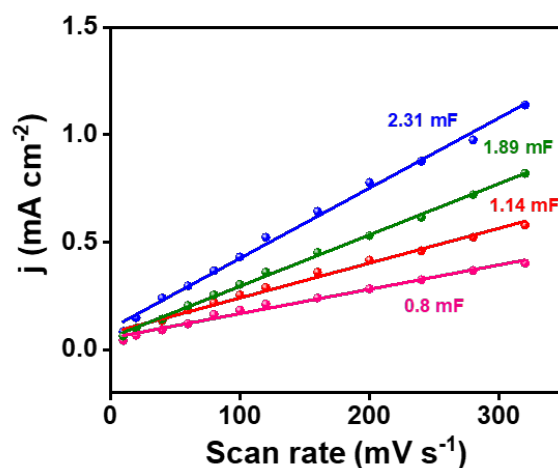
Fig. S10 Comparison of C_{dl} values of different catalysts extracted from Fig. S9 (Pink: Ni$_4$B$_3$, Blue: Cu-Ni$_4$B$_3$ (1:2), Green: Cu-Ni$_4$B$_3$ (2:1) and Red: Cu-Ni$_4$B$_3$ (1:1)).

**Fig. S11** Powder X-ray diffraction patterns for Ni$_4$B$_3$ and as-synthesized Cu-Ni$_4$B$_3$ catalysts.
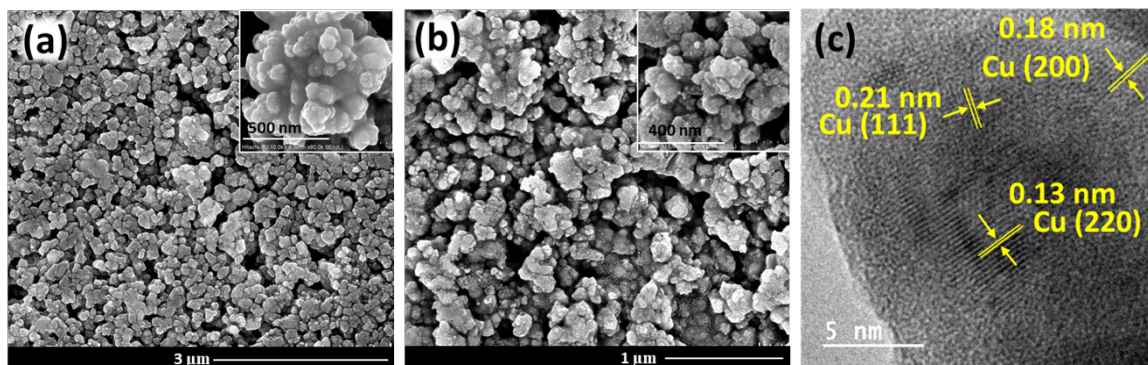
Fig. S12 FE-SEM images of (a) Cu-Ni$_4$B$_3$ (1:1) and (b) Cu-Ni$_4$B$_3$ (2:1) catalyst at different magnifications. (c) HR-TEM image of Cu-Ni$_4$B$_3$ (1:2) catalyst.
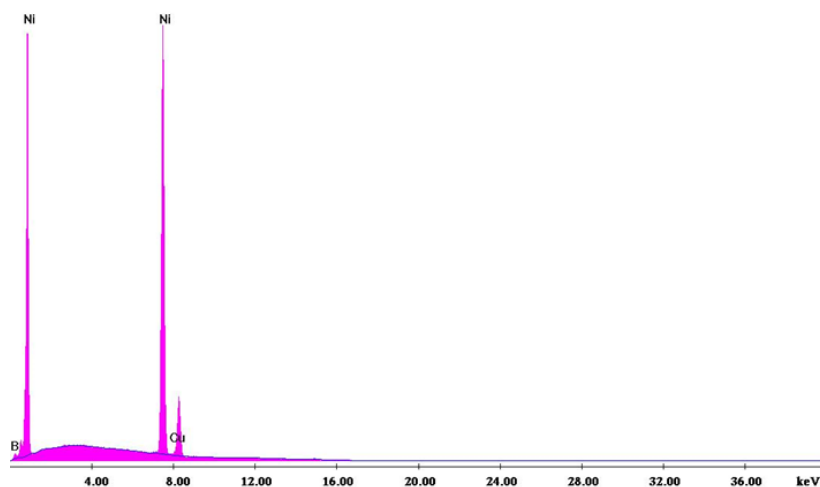

Fig. S13 EDS spectrum showing presence of Ni, Cu and B elements.

Table S5. MP-AES analysis for Cu-Ni$_4$B$_3$ (1:2) catalyst.

| Catalyst	Metal	Sample wt.	Volume	Concentration	Metal (mass %)
Cu-Ni$_4$B$_3$ (1:2)	Ni	5 mg	50 mL	30.81	30.81
Cu-Ni$_4$B$_3$ (1:2)	Cu	5 mg	50 mL	18.21	18.21
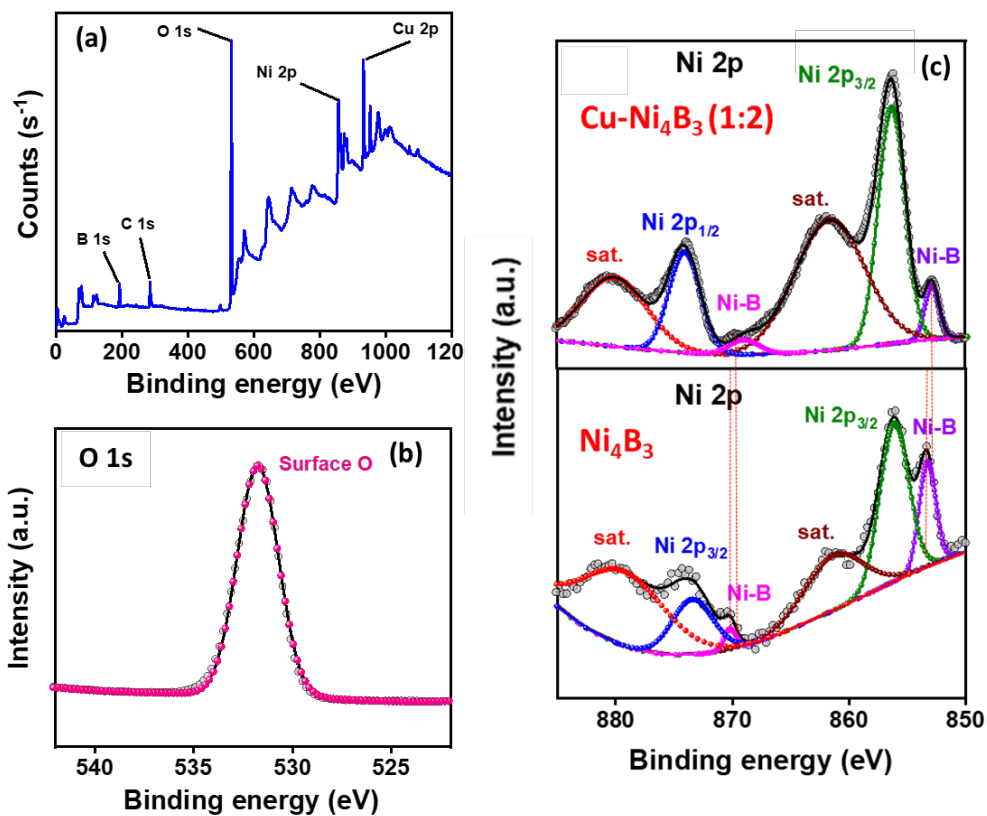
Fig. S14 (a) XPS survey spectrum and (b) O 1s spectrum for Cu-Ni$_4$B$_3$ (1:2) catalyst. (c) Comparison of Ni 2p XP deconvoluted spectrum for Ni$_4$B$_3$ and Cu-Ni$_4$B$_3$ (1:2) catalyst.
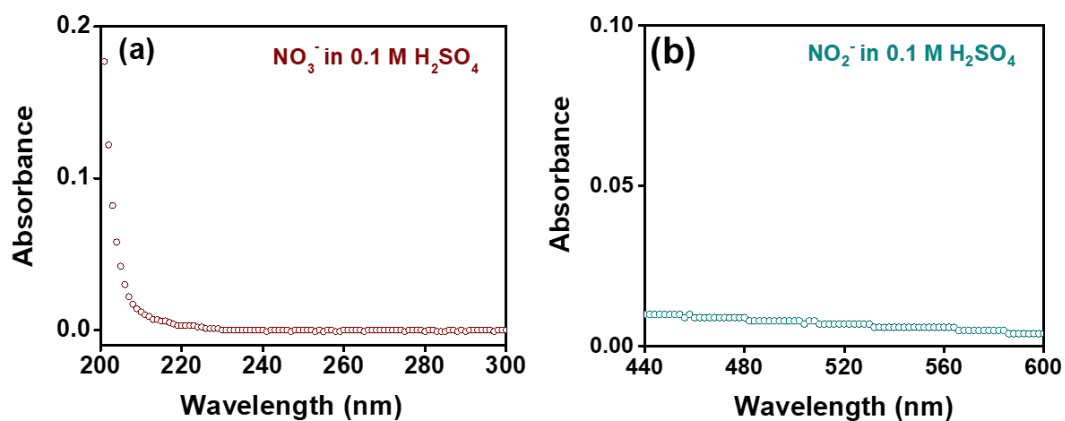
Fig. S15 UV-Vis absorbance curves obtained in 0.1 M H$_2$SO$_4$ electrolyte for the detection of (a) NO$_3^-$ and (b) NO$_2^-$ in turn.
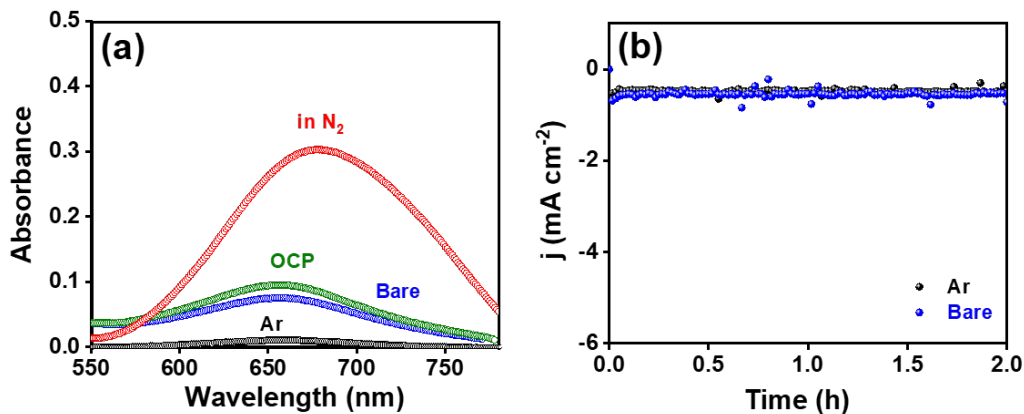
Fig. S16 (a) UV-Vis absorbance curves for samples collected after control NRR experiments and (b) respective chronoamperometry curves.
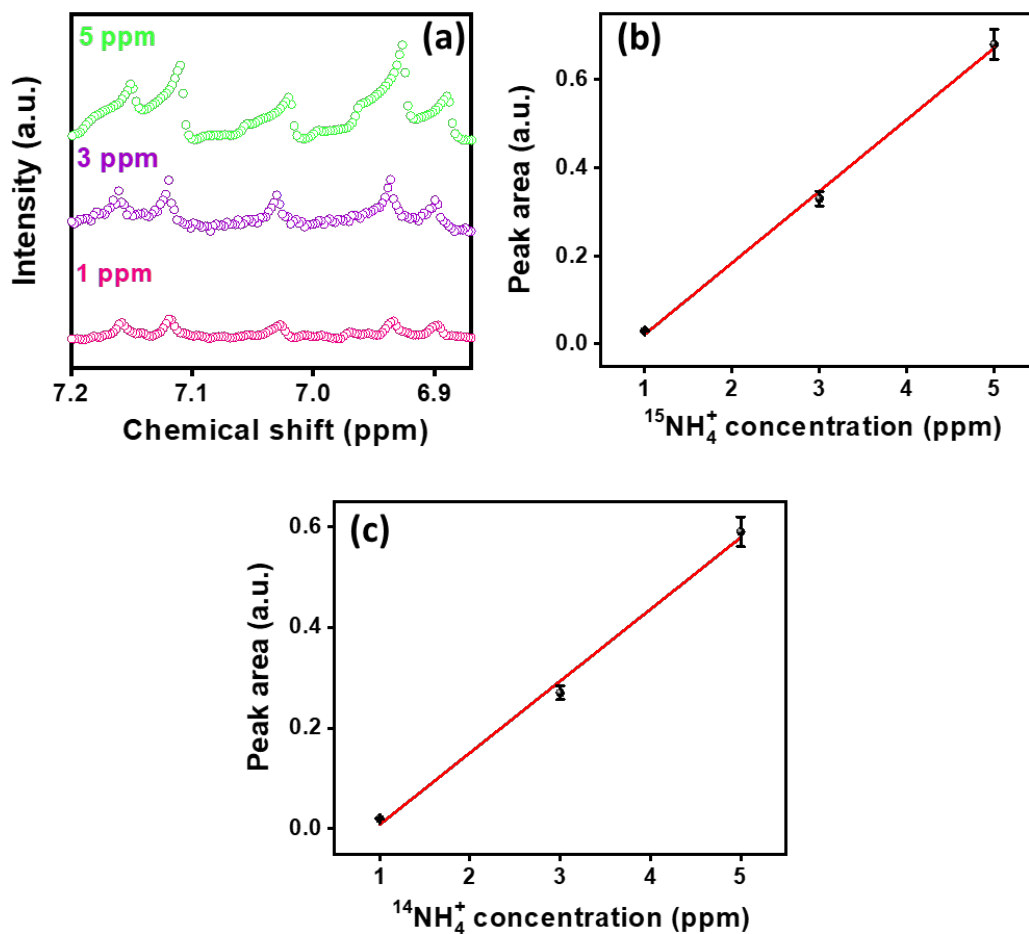
Fig. S17 (a) ^{1}H-NMR spectrum for standard $^{14}NH_4^+$ and $^{15}NH_4^+$ samples of known concentrations and (b-c) relative calibration curves extracted from the same.
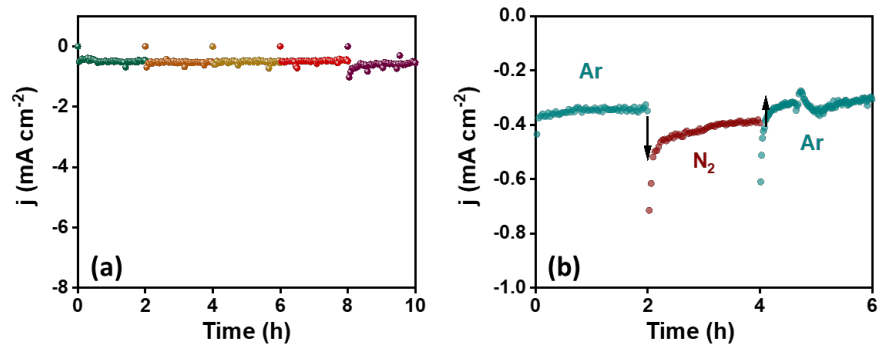
Fig. S18 (a) CA measurements executed for 10 h under N_2-saturated 0.1 M H_2SO_4 electrolyte and (b) under switching gas-feed environments for 2 h each at -0.3 V by Cu-Ni_4B_3 (1:2) catalyst.
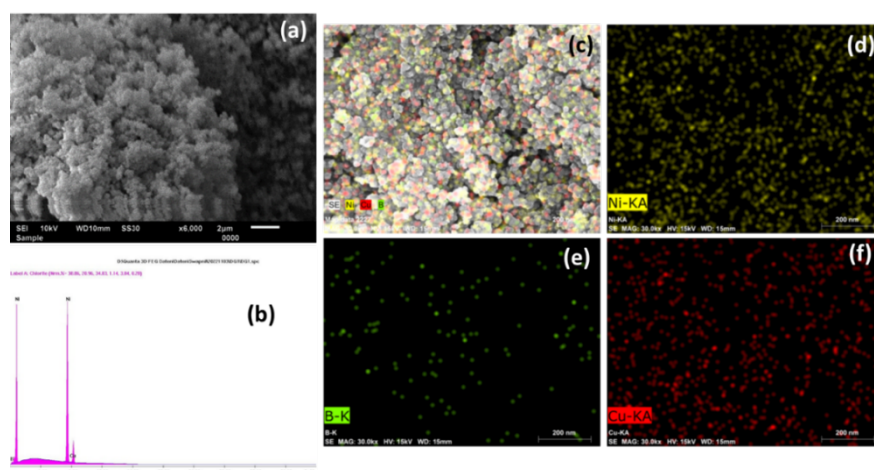
Table S6. MP-AES analysis for Cu-Ni_4B_3 (1:2) catalyst after NRR stability tests.

Catalyst	Metal	Sample wt.	Volume	Concentration	Metal (mass %)
Cu-Ni_4B_3 (1:2)	Ni	5 mg	50 mL	30.05	30.05
Cu-Ni_4B_3 (1:2)	Cu	5 mg	50 mL	17.96	17.96

Fig. S19 (a) FE-SEM image and (b) EDS spectrum of Cu-Ni_4B_3 (1:2) catalyst after NRR stability measurements, (c-f) EDS dot mapping images obtained for Cu-Ni_4B_3 (1:2) catalyst showing presence and uniform distribution of all the expected elements in scanned area.

References

1. D. Gupta, A. Kafle, S. Kaur, P. Parimita Mohanty, T. Das, S. Chakraborty, R. Ahuja and T. C. Nagaiah, *J. Mater. Chem. A*, 2022, **10**, 20616-20625.
2. H. Ren, Y. Pan, C. C. Sorrell and H. Du, *J. Mater. Chem. A*, 2020, **8**, 3154-3159.
3. J. Han, X. Ji, X. Ren, G. Cui, L. Li, F. Xie, H. Wang, B. Li and X. Sun, *J. Mater. Chem. A*, 2018, **6**, 12974-12977.
4. C. Li, S. Mou, X. Zhu, F. Wang, Y. Wang, Y. Qiao, X. Shi, Y. Luo, B. Zheng and Q. Li, *Chem. Commun.*, 2019, **55**, 14474-14477.
5. W. Zang, T. Yang, H. Zou, S. Xi, H. Zhang, X. Liu, Z. Kou, Y. Du, Y. P. Feng and L. Shen, *ACS Catal.*, 2019, **9**, 10166-10173.
6. L. Yang, T. Wu, R. Zhang, H. Zhou, L. Xia, X. Shi, H. Zheng, Y. Zhang and X. Sun, *Nanoscale*, 2019, **11**, 1555-1562.
7. K. Ba, G. Wang, T. Ye, X. Wang, Y. Sun, H. Liu, A. Hu, Z. Li and Z. Sun, *ACS Catal.*, 2020, **10**, 7864-7870.
8. C. Guo, X. Liu, L. Gao, X. Kuang, X. Ren, X. Ma, M. Zhao, H. Yang, X. Sun and Q. Wei, *Appl. Catal. B Environ.*, 2020, **263**, 118296.
9. X. Ji, T. Wang, Q. Liu, Y. Luo, S. Lu, G. Chen, S. Gao, A. M. Asiri and X. Sun, *EcoMat*, 2020, **2**, e12026.
10. L. Zhang, M. Cong, X. Ding, Y. Jin, F. Xu, Y. Wang, L. Chen and L. Zhang, *Angew. Chem.*, 2020, **132**, 10980-10985.
11. S. Li, Y. Wu, Q. Liu, B. Li, T. Li, H. Zhao, A. A. Alshehri, K. A. Alzahrani, Y. Luo and L. Li, *Inorg. Chem. Front.*, 2021, **8**, 3105-3110.
12. X. Yang, Y. Ma, Y. Liu, K. Wang, Y. Wang, M. Liu, X. Qiu, W. Li and J. Li, *ACS Appl. Mater. Interfaces*, 2021, **13**, 19864-19872.
13. L. Han, M. Hou, P. Ou, H. Cheng, Z. Ren, Z. Liang, J. A. Boscoboinik, A. Hunt, I. Waluyo and S. Zhang, *ACS Catal.*, 2020, **11**, 509-516.
14. K. Chu, Y. Luo, P. Shen, X. Li, Q. Li and Y. Guo, *Adv. Energy Mater.*, 2022, **12**, 2103022.
15. D. Johnson, B. Hunter, J. Christie, C. King, E. Kelley and A. Djire, *Sci. Rep.*, 2022, **12**, 1-10.
16. Y. Kong, Y. Li, X. Sang, B. Yang, Z. Li, S. Zheng, Q. Zhang, S. Yao, X. Yang and L. Lei, *Adv. Mater.*, 2022, **34**, 2103548.
17. H.-j. Chen, Z.-q. Xu, S. Sun, Y. Luo, Q. Liu, M. S. Hamdy, Z.-s. Feng, X. Sun and Y. Wang, *Inorg. Chem. Front.*, 2022, **9**, 4608-4613.
18. Q. Liu, Y. Lin, S. Gu, Z. Cheng, L. Xie, S. Sun, L. Zhang, Y. Luo, A. A. Alshehri and M. S. Hamdy, *Nano Res.*, 2022, **15**, 7134-7138.
19. J. Chen, Y. Kang, W. Zhang, Z. Zhang, Y. Chen, Y. Yang, L. Duan, Y. Li and W. Li, *Angew. Chem. Int. Ed.*, 2022, **61**, e202203022.
20. X. Peng, R. Zhang, Y. Mi, H. T. Wang, Y. C. Huang, L. Han, A. R. Head, C. W. Pao, X. Liu and C. L. Dong, *ChemSusChem*, 2023, **16**, e202201385.
21. M. Sun, C. Ma, M. Ma, Y. Wei, S. Dong, X. Zhang, J. Tian and M. Shao, *Mater. Today Phys.*, 2023, **30**, 100945.
22. C. M. Sánchez-Sánchez, J. Rodríguez-López and A. J. Bard, *Anal. Chem.*, 2008, **80**, 3254-3260.